A novel hybrid microrobot using rotational magnetic field for medical applications

Qiang Fu · Shuxiang Guo · Yasuhiro Yamauchi ·
Hideyuki Hirata · Hidenori Ishihara

Abstract Magnetically actuated microrobots for such tools have potential accomplish procedures in biological and medical applications. In this paper, a novel magnetically actuated hybrid microrobot with hybrid motion driven by an electromagnetic actuation system has been proposed. An o-ring type permanent magnet is embedded in the hybrid microrobot as an actuator driven by rotational magnetic field which is generated by a 3 axes Helmholtz coils. It is composed by two motion mechanisms. One is the spiral jet motion moved by rotating its body. The other one is fin motion moved by vibrating its body. Because only one permanent magnet is used inside the hybrid microrobot, two motions can be controlled separately without any interference. The hybrid microrobot can change its two motions to realize multi-DOFs movement and flexibility motion. The verified experiments are conducted in the pipe. The experimental results indicate that the moving speed can be controlled by adjusting the magnetic field changing frequency and the direction of motion can be controlled by changing the magnetic field direction.

Q. Fu (✉) · Y. Yamauchi
Graduate School of Engineering, Kagawa University, 2217-20, Hayashi-cho, Takamatsu 761-0396, Japan
e-mail: fuqiang252@gmail.com

S. Guo · H. Hirata · H. Ishihara
Faculty of Engineering, Kagawa University, 2217-20, Hayashi-cho, Takamatsu 761-0396, Japan

S. Guo
e-mail: guo@eng.kagawa-u.ac.jp

S. Guo
School of Life Science, Beijing Institute of Technology, 5 South Zhongguancun Street, Haidian District, Beijing 100081, China

1 Introduction

The endoscope as a helpful tool for medical applications typically refers to inspect the interior of the body in medical procedures (Guo et al. 2002 and 2003; Behkam and Sitti 2005; Nacci et al. 2008; Yu et al. 2010; Mir-Nasiri and Siswoyo Jo 2011; Yim and Sitti 2012; Guo et al. 2014). The first endoscope was developed by Philipp Bozzini (1806). The endoscope was made by Lichtleiter (light conductor) for examination of the interior of a hollow organ in the human body. In the 1960s, the first fiberoptic endoscope consisting of a bundle of flexible glass fibres was invented by Basil Hirschowitz and Larry Curtiss. It has the ability to coherently transmit an image and becomes a vital tool for diagnosing gastrointestinal (GI) diseases. There were physical limits to the image quality of a fibroscope. The electronic endoscope became more popular with the development of the electronic technology. Doctors can monitor intestinal image *via* the display and perform examination, rather than staring at eyepiece. Generally, these endoscopes are used to examine inside a large intestine. However, they brought much painful and traumatic due to being driven by a cable or tube. Especially, they are hard to carry deeply to some small or narrow areas within the tissue of living in human body. To solve these problems, different kinds of wireless capsule endoscopes (WCEs) have been developed (Moglia et al. 2007; Wang and Meng 2011; Basar et al. 2012). These WCEs are mainly consisted by an embedded camera, image sensor and battery for power supply. They are swallowed by the patient and travel through the gastrointestinal tract. Then it transmits images towards a monitor outside the body. In general, the time for medical

procedure is about 8 h. After examination, the capsule is excreted naturally from the anus. In addition, several companies also developed some capsule endoscopes which are used for diagnosis of different GI parts, such as Norika, Olympus and so on. Conversely, compared with traditional endoscopes, these capsule endoscopes cannot allow the operator to realize flexible control in the GI tract, due to their movement depend on the peristalsis of intestines.

At present, researchers have proposed different kinds of control method to address this problem. One is internal control method and the other is external control (remote motion control). Generally, the motors (Wang et al. 2005), shape memory alloy SMA (Kim et al. 2005) actuators or ICPF actuators (Gao et al. 2011) are utilized to realize internal control for the capsule endoscope. They require inner power or a line from an external power source. But it is still difficult to develop a microrobot with compact structure, flexible locomotion and long-distance movement by power supply, because the three characteristics conflicts each other. A number of researchers have proposed numerous microrobotic control methods utilizing the magnetic field to realize remote motion control (Honda et al. 2001; Pan and Guo 2007; Zhang et al. 2009; Jeong et al. 2012; Guo et al. 2013; Fu et al. 2014). The reason is that it can integrate the components for motion control and wirelessly power supply inside microrobot. In particular, the use of magnetic field for microrobot control is increasing. The mechanisms and structures of the microrobot are different due to using the different type of magnetic field. Yesin et al. (2006a and b) proposed a kind of magnetic microrobot. This kind of microrobot is driven by a gradient magnetic field generating the pushing and pulling force to the microrobot. However, the magnetic field strength for locomotion depends on the microrobot materials, volume and environment. Pan et al. (2011) developed a type of wireless microrobot utilizing an elastic tail which is driven by an alternating magnetic field. However, because of the structural limitation of the control system, the microrobot is hard to realize changing its motion direction. Another control method is using the rotational magnetic field which generates a rotational motion (Pan and Guo 2009; Okada et al. 2012a). For example, Choi et al. (2009) developed an EMA system which consists of Helmholtz and Maxwell coils. The microrobot can move in the 2-D surface in this system. However, most of microrobots based on a rotational magnetic field can only realize a single motion. Therefore, locomotion of the microrobots is limited by changes in the environment due to their structure. In this paper, a novel type of magnetically actuated hybrid microrobot (MAHM) based on a rotational magnetic field is proposed. The hybrid microrobot with spiral jet motion and fin motion has a

small scale with a wireless power supply, can be propelled by low voltage, and has a quick response. And also the hybrid microrobot can work for a long time in human. It can convert its two motions (spiral jet motion and fin motion) through the proposed structure of the microrobot with rotational magnetic field, so that it realizes the movement in the different environment. The body of the microrobot with a spiral jet motion can obtain a stable motion and high propulsive force than the spiral motion. The fin motion can improve the dynamic characteristic and reduce the shake which caused by the axial propulsive force of the spiral jet motion. Spiral motion and fin motion can be controlled separated without any interference, due to the hybrid microrobot has only use one actuator to realize the spiral jet motion and fin motion. The 3 axes Helmholtz coils is used to generate the rotational magnetic field in any direction, which is used to provide a magnetic torque for controlling the microrobot at the workspace. The experimental results indicated the hybrid microrobot can change its two motions to realize multi-DOFs movement and flexibility motion in the pipe. In addition, the moving speed is controlled by adjusting the magnetic field changing frequency and the direction of motion is controlled by changing the magnetic field direction.

A whole microrobot control system is illustrated in Section 2. A novel magnetically actuated hybrid microrobot with hybrid locomotion is developed in Section 3. Electromagnetic actuated methods for the hybrid microrobot is discussed in Section 4. Section 5 describes the experimental assessment to confirm performance of hybrid motion and flexibility. Finally, conclusions and future works are illustrated.

2 Conceptual design of the whole control system

Generally, the patients are placed on a liquid diet starting after lunch the day before the examination. And then, the patients should be drink the poly tetramethylene ether glycol 2000 ml and water 500 ml, 2~4 h before examination. After all preparations, the microrobot is swallowed inside the digestive organs and can be manipulated (Moglia et al. 2007; Keller et al. 2012). Conceptual diagram of the whole microrobotic control system is shown in Fig. 1. The control system consists of a magnetically actuated hybrid microrobot, magnetic sensor array, three axes-Helmholtz coils, CT-Scan, monitor, and operation device (Phantom Omni device). Firstly, an intestinal image is generated by the CT scanner and the doctor views the intestinal image to confirm the area of a target in a monitor. Secondly, the doctor operates the Phantom

Fig. 1 Conceptual diagram of the whole control system
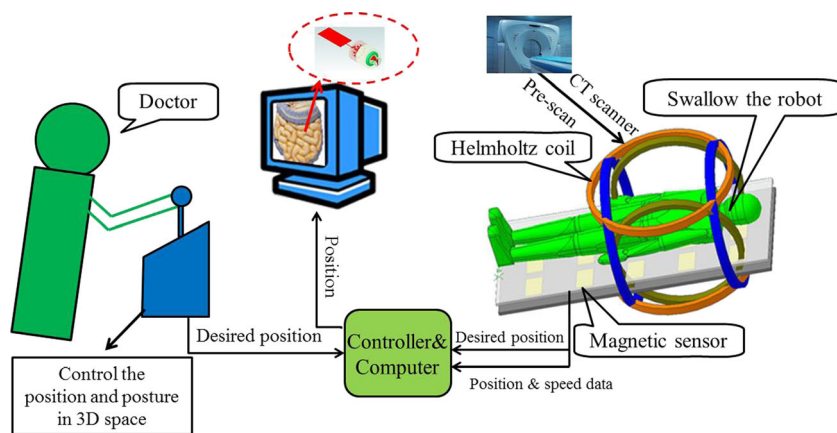
Omni device to control the magnetically actuated hybrid microrobot to move to the target by using an external magnetic field. A 3 axes Helmholtz coils is used to generate the external rotational magnetic field. When the hybrid microrobot arrives at the target area, the operator controls the position and posture of the hybrid microrobot to detect or treat disease in an intestinal tract. Meanwhile, the monitor shows the real time position and position of the hybrid microrobot calculated from the measurement data of magnetic sensor array. The magnetic sensor array is used to realize the close-loop control and ensure the hybrid microrobot to reach the target location.

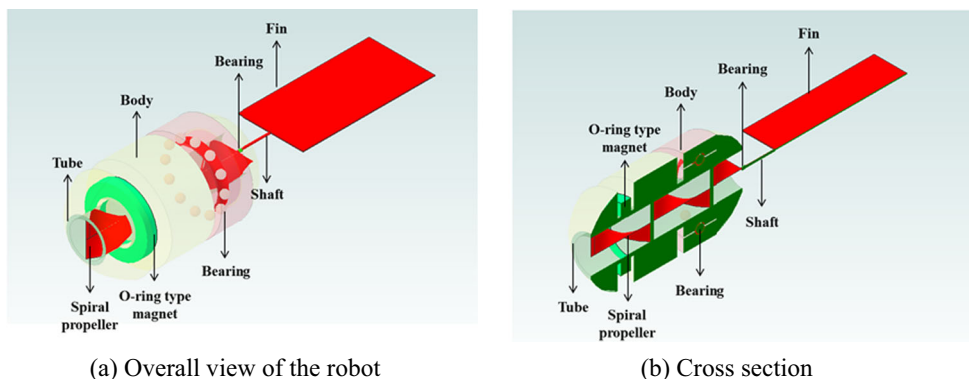## 3 Magnetically actuated hybrid microrobot design

3.1 Concept of the magnetically actuated hybrid microrobot

A novel type of magnetically actuated hybrid microrobot (MAHM) with compact and efficient structure is proposed, as shown in Fig. 2. The prototype of magnetically actuated hybrid microrobot is illustrated in Fig. 3. The specification is given in Table 1. The spiral propeller is connected to a tube. An o-ring type permanent magnet is assembled at the front end of the tube and a bearing is assembled at the back end of the tube. Inner ring of bearing connects to the tube and outer ring of bearing is fastened inside the body. The fin is connected to the back end of the propeller with a bearing and a shaft. When the microrobot moves with the spiral jet motion, the outer shell of the microrobot is not rotates, it can be reduce damage for the intestinal wall and the fin can improve the dynamic characteristic and reduce the shake caused by the axial traction force at the spiral jet motion.

3.2 Motion mechanism of the magnetically actuated hybrid microrobot

The MAHM has two motion mechanisms. One is the spiral jet motion which can move by rotating the spiral propeller. The other is fin motion which can move by vibrating the fin. The MAHM can switch between the two motions to realize movement in various working environments. The spiral jet motion is used when the microrobot needs precision operation and stable movement. The fin motion is used when the high propulsive

Fig. 2 Conceptual design of magnetically actuated hybrid microrobot (MAHM)

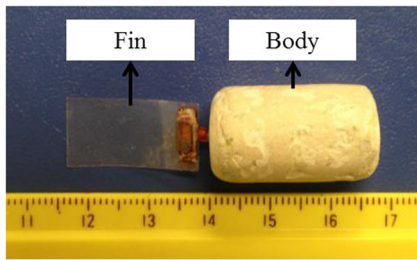(a) Overall view of the robot   (b) Cross section

Fig. 3 Prototype of magnetically actuated hybrid microrobot (MAHM)

force is needed. Due to just only use one magnet inside the MAHM, two motions can be controlled separately without any interference. It can obtain rapid responsive than the robot (Okada et al. 2012b).

Based on the magnetic theory, rotation of the microrobot in an external magnetic field requires at least a pair of forces in opposite directions, and a torsional moment should be generated. The microrobot is rotated due to an embedded inner o-ring type magnetic with radial magnetization, and the axial propulsive force is generated by pushing the fluid backward to obtain the forward motion due to the reaction force. Fig. 4a shows the principle of bi-directional movement with spiral jet motion according to changes in rotational direction of the magnetic field. When the rotational direction of the magnetic field is clockwise (CW), the microrobot generates a forward propulsive force and the microrobot moves forwardly. When the rotational direction of the magnetic field is counter-clockwise (CCW), the microrobot generates a backward propulsive force and the microrobot moves backwardly. In addition, when an alternate magnetic field parallel to the direction of advance is applied, movement due to an impelling force arising from a permanent magnet rotates and vibrates the connected fin as shown in Fig. 4b. The rotational movement is shown in Fig. 5. When the plane of the rotational magnetic field is CCW, the microrobot can turn left at a branch point. When the plane of the rotational magnetic field is CW, the microrobot can turn right at a branch point. Therefore, the velocity of the hybrid microrobot can be controlled by adjusting the rotational magnetic field changing frequency. And the

Table 1   Specification of the magnetically actuated hybrid microrobot

Magnetically actuated hybrid microrobot			
Length	Diameter	Weight	Material
51 mm	14 mm	3.56 g	Polystyrene
O-ring type magnet			
Outer diameter	Internal diameter	Height	Material
9.5 mm	5.1 mm	1.5 mm	Neodymium

direction of motion can be controlled by changing the rotational magnetic field direction.

3.3 The principle of spiral Jet motion

The propulsive force model of the spiral jet motion is shown in Fig. 6. According to the fluid mechanics, spiral jet propulsive mechanism is analyzed. The velocity of the outflow is given by Eq. (1).

$$v_2 = v_1 + \frac{A_1 \cdot v_1}{A_2} = v_1 + \frac{Q}{A_2} \tag{1}$$

Flow for the spiral jet motion is calculated by Eq. (2).

$$Q = a \cdot b \cdot \sqrt{p^2 + (2\pi r)^2} \cdot \Omega \tag{2}$$

The propulsive force of the spiral jet motion is obtained indicated in Eq. (3):

$$F_{spiral} = \rho \cdot A_2 \cdot v_2^2 - \frac{1}{2} \cdot C_D \cdot \rho \cdot A \cdot v_2^2 \tag{3}$$

Where, F_{spiral} is the propulsive force of the microrobot. v_1 is velocity of the inflow. v_2 is velocity of the outflow. Q is the flow for the spiral jet motion. a is the height of the spiral ditch and b is the width of the spiral ditch. p is the pitch of the spiral, and r is the radius of the robot's width. Ω is the speed of revolution. A is the cross section of the body. A_1 is the cross section of the inflow. A_2 is the cross section of the outflow. The simulation results are shown in Fig. 7.

The propulsive forces for various frequencies were measured using a measurement setup which mainly consists of a laser displacement sensor and a copper beam and electric balance (Pan 2008), as shown in Fig. 8. The copper beam was soft enough to bend under the propulsive force and the propulsive force is evaluated by the electric balance. The displacement of copper beam and propulsive force are able to be considered as right triangle. According to the measurement of displacement (x) and the force (F), a calibration calculation of relationship between the propulsive force the bending displacement of the copper beam is obtained as shown in Eq. (4).
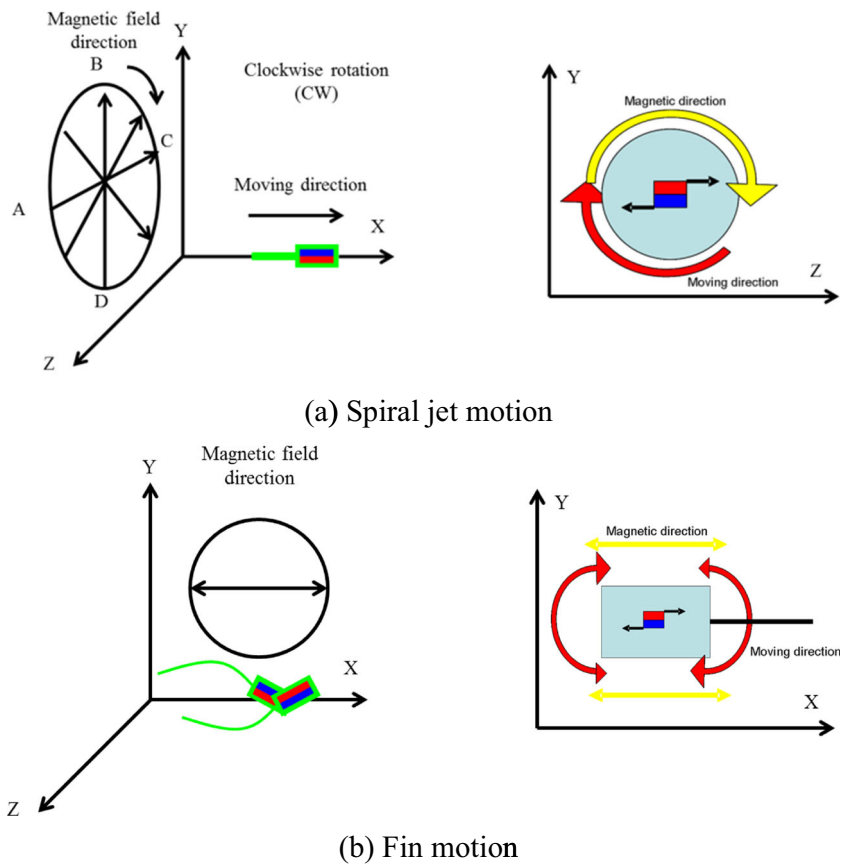
$$F = 1.354 \times x \tag{4}$$

where, x is the bending displacement of the copper beam measured by a laser sensor and F is the propulsive force.

Fig. 4 Bi-directional movement (**a**) Spiral jet motion (**b**) Fin motion

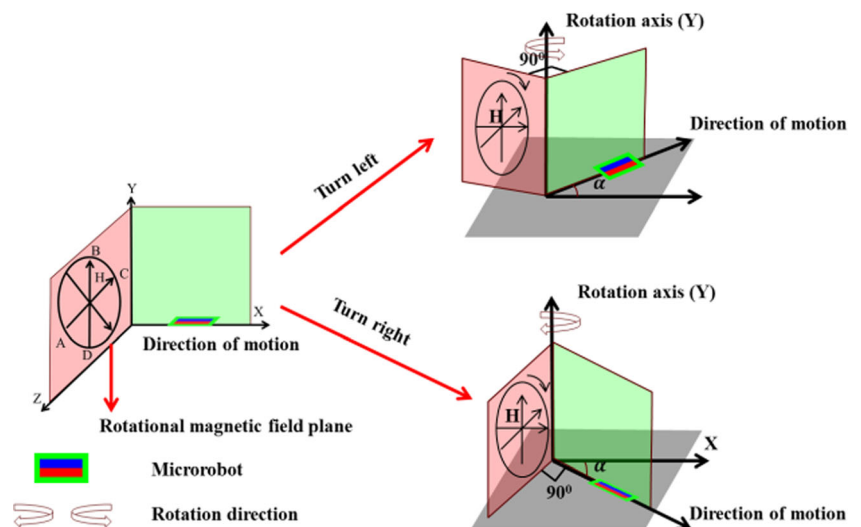(a) Spiral jet motion

(b) Fin motion

During the testing experiment of the propulsive force, the microrobot was placed in the pipe which was filled the water. And then, by adjusting the frequency of input electric currents to control the rotating speed of the body, the displacement of the copper beam was obtained by the laser sensor. At last, the calibration calculation equation is used to calculate the propulsive force. Measurement results of mean propulsive force are shown in Fig. 9a. In experiment condition, the experimental results are smaller than the simulation results due to drag force of the water. This tendency is similar to the simulation results. The Fig. 9b shows the measurement results of speed. The experimental result indicates speed of the microrobot became more faster with the frequency increasing.

3.4 The principle of Fin motion

According to Vortex Peg Hypothesis, the fish uses tail or fin to propel itself forward by thrusting its body against the
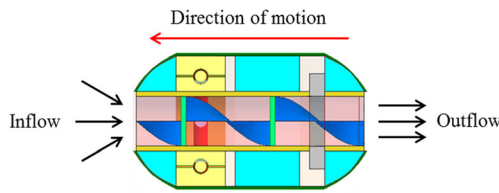
Fig. 5 Rotational movement

Fig. 6 Propulsive force model of the spiral jet motion

seemingly fixed vortices and utilizing their rotational energy. The placement and direction of these vortices indicate that the wake structure generated by the fin takes the form of a series of parallel waves or a reverse Karman vortex street which is indicative of thrust generation. The velocity field induced by this wake structure expels a jet of water in the downstream direction, propelling the fin forward to conserve momentum. Then, thrust of fish-like robot generated by the added mass and vorticity methods combine to yield the total propulsive force. In previous study, we have discussed that the undulatory motion of the tail which can obtain good performances is better than the oscillatory motion. Therefore, the undulatory motion is used to generate the thrust for the microrobot. A model of the tail with fin motion is shown in Fig. 10. The total propulsive force (F_{fin}) of fin motion and normal force (N) are indicated in Eqs. (5) (6) (7).

$$F_{Fin} = \int_{\frac{-b(f)}{2}}^{\frac{b(f)}{2}} t\,dy = \int_{\frac{-b(f)}{2}}^{\frac{b(f)}{2}} (L\sin\alpha - D\cos\alpha)\,dy \quad (5)$$

$$N = \int_{\frac{-b(f)}{2}}^{\frac{b(f)}{2}} n\,dy = \int_{\frac{-b(f)}{2}}^{\frac{b(f)}{2}} (L\cos\alpha + D\sin\alpha)\,dy \quad (6)$$

The induced flow angle (α) is

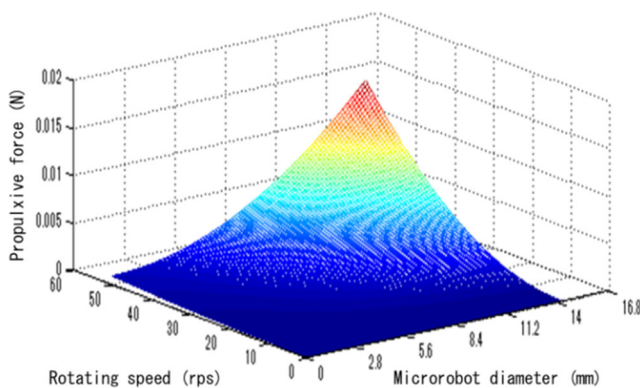$$\alpha = \tan^{-1}\left(\frac{V_x}{V_z}\right) \quad (7)$$
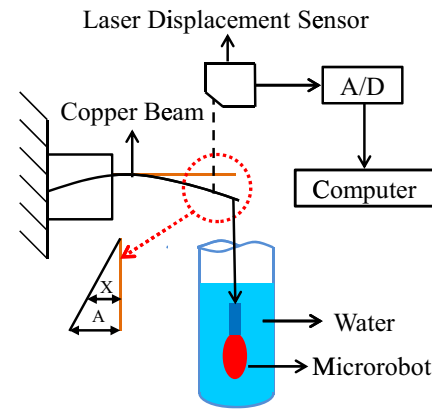

Fig. 7 Simulation results of propulsive force

Fig. 8 Measurement system of the propulsive force

where, t is propulsive force. n is normal force. V_x is velocity of the x direction and V_z is velocity of the z direction. The displacement b is a function of the frequency (f).

Using Eqs. (5) (6) (7), the power is calculated, as follows Eq. (8):

$$P = \int_{\frac{-b}{2}}^{\frac{b}{2}} \left(nh' - mk'\right)dy = \int_{\frac{-b}{2}}^{\frac{b}{2}} \left[h'(L\cos\alpha + D\sin\alpha) - mk'\right]dy \quad (8)$$

where, h is the heaving motion of the fin. k is the feathering movement of the fin.

The mechanical efficiency η is calculated by Eq. (9):

$$\eta = \frac{F_{Fin}V}{P} = \frac{C_T}{C_P} \quad (9)$$

where, C_T is propulsive coefficient and C_P is power coefficient.

The resonance frequency of the fin motion is confirmed by Eqs. (10) (11) and (12). Assuming the beam deflection for the transverse vibration, the transverse vibration of fin is calculated by Eq. (10). The conditional expression by using fixed end is shown in Eq. (11).

$$EI\frac{\partial^4 y}{\partial x^4} + \rho A\frac{\partial^2 y}{\partial t^2} = 0 \quad (10)$$

$$1 + \cos\beta \cdot \cosh\beta = 0 \quad (11)$$

The resonance frequency (f) of the fin can be calculated as follows (12):

$$f = \frac{\beta}{2\pi}\frac{1}{L^2}\sqrt{\frac{EI}{\rho A}} \quad (12)$$

where, β is characteristic value, E is young's modulus of the fin, I is second moment of area, L is length of the fin, ρ is density, A is cross section of the fin. The relationship between resonance frequency and displacement of fin is measured with measurement system. Figure 11 shows the experimental results that the
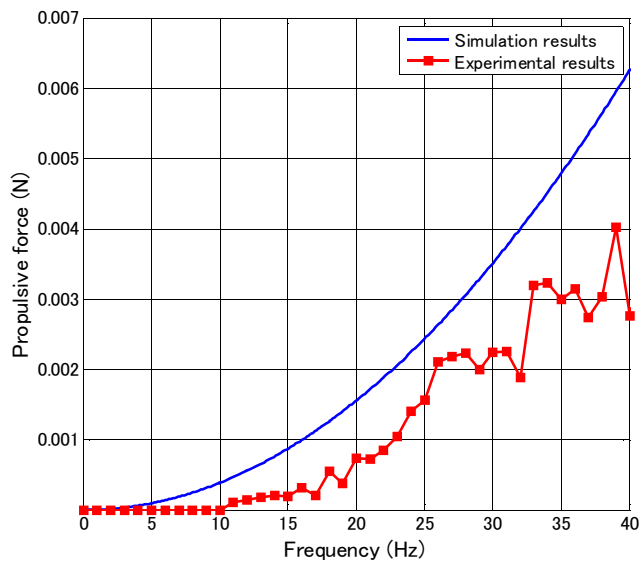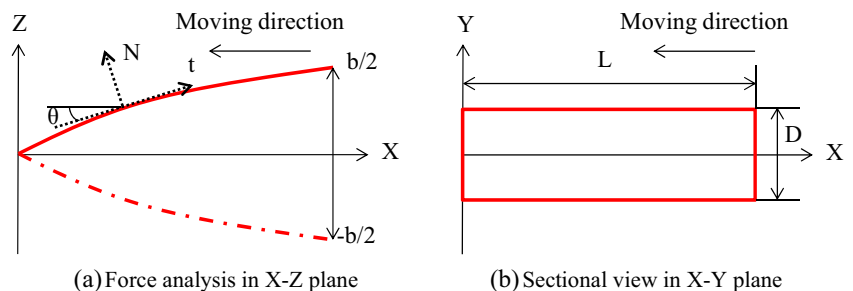
(a) Measurement results of propulsive force
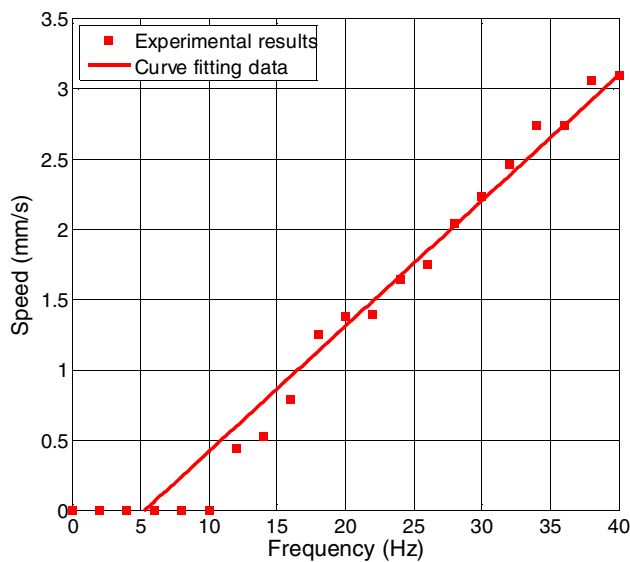
(b) Measurement results of speed

Fig. 9 Measurement results (**a**) Measurement results of propulsive force (**b**) Measurement results of speed

maximum displacement of the fin with the same width and the different length is measured. The resonance
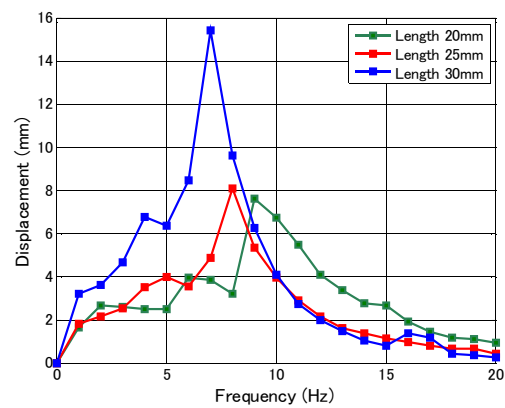

Fig. 11 Relationship between frequency and displacement of fin with different length

frequency is from 0 to 20 Hz. And maximum displacement was obtained at 7 Hz.Figure 12 shows the experimental results that the performance of the fin motion with different materials. One is the fin which is made of polyethylene terephthalate (PET). The other is the fin which is made of ethylene-vinyl acetate (EVA) and PET. The size is constant which is 20 mm*10 mm*0.1 mm. It indicated the fin which is composed by PET and EVA obtained higher moving speed and wider frequency than the fin which is made by PET. Because the former is softer than the latter, the former one can realize the higher moving speed with the undulatory motion better. Therefore, the former is utilized for the microrobot in our research.

4 Force analysis of microrobot

When the microrobot moves in the fluid, the force consists of propulsive force, hydraulic resistance buoyancy and gravity. Motion equations of the microrobot are given in Eqs. (13) and (14).

$$Ma = F_{spiral} + F_{Fin} - F_D + F_\rho\cos\gamma - Mg\cos\gamma \qquad (13)$$

$$F_D = \frac{1}{2} \times C_D \times \rho \times A \times v^2 + 2 \times C \times \pi r\omega L \qquad (14)$$

Fig. 10 The model of tail with fin motion

(a) Force analysis in X-Z plane
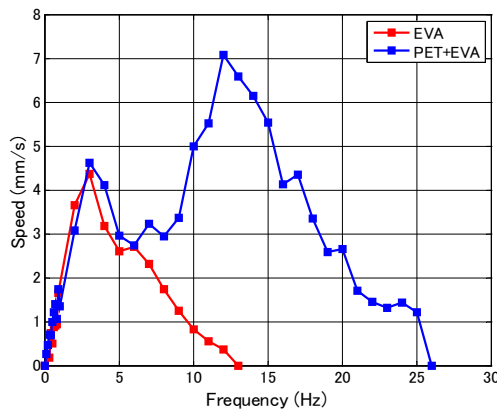

(b) Sectional view in X-Y plane

Fig. 12 Relationship between frequency and moving speed with different materials

where, M is the mass of the microrobot. C_D is the coefficient of resistance. ρ is fluid density. a is acceleration. F_D is total resistance. A is projected area. γ is angle with horizontal plane. L is the length of the microrobot.

The magnetic field applies a magnetic torque for the microrobot to produce the propulsive force. The magnetic force F_M and magnetic torque T_M acting on the o-ring magnet in the external magnetic field of the 3 axes Helmholtz coils is given by the Eqs. (15) and (16):

$$F_M = \mu_0 V (M \cdot \nabla) H \times \sin\alpha \tag{15}$$

$$T_M = \mu_0 V M \times H \times \sin\alpha \tag{16}$$

where, M is the average magnetization of the internal magnet and V is the volume of the internal magnet. H is magnetic field intensity. α is the angle of between M and H.

The rotating torque T_R is calculated by Eq. (17),

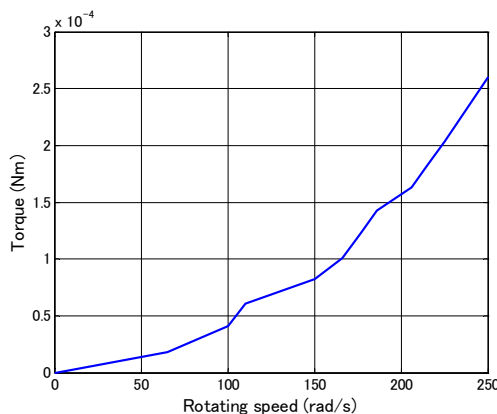$$T_R = I \times \theta'' + C \times \theta' \tag{17}$$

Fig. 13 Relationship between rotating speed and torque

where, I is moment of inertia, C is coefficient of viscosity friction, θ is rotational angle. During the measurement experiment, we adjusted the frequency of input electric currents to control the rotating speed of the microrobot. The torque was measured by the torque sensor at the same time. The relationship between rotating speed and rotation torque is measured, as shown in Fig. 13.

5 Experimental results

The experimental setup and the schematic diagram are shown in Fig. 14. The hybrid microrobot is placed in a transparent pipe with diameter 26 mm. The transparent is filled with water (water density: 998.203 kg/m^3) at temperature 22 °C and inserted 3 axes Helmholtz coils. The web camera will monitor inside of pipe and generate a visual image on the display. Meanwhile, the operator operates the Phantom Omni device to control the position and posture of the hybrid microrobot while viewing the display. The display shows the data to obtain the real-time position of the robot. The drive signals are generated by Phantom Omni device and sent to the 3 axes Helmholtz coils to control the hybrid microrobot. The magnetic flux density changing frequency is shown by oscilloscope.

### 5.1 Multi-DOF locomotion of the hybrid microrobot

Using the experimental setup, the multi-DOF locomotion of the hybrid microrobot is to be tested in the pipe. The microrobot realized multi-DOFs locomotion by this spiral jet motion and fin motion. The microrobot moves forward-backward and stops by changing the rotational uniform magnetic field. Additionally, it is confirmed the microrobot has equivalent moving speed even backward by experiment. Experimental results of the hybrid motion in a horizontal direction are shown in Fig. 15. Experimental results of the moving state of the microrobot in vertical direction are shown in Fig. 16. Based on experimental results, the hybrid microrobot realized the movement in the horizontal plane and vertical plane by adjusting rotational magnetic field.

Experiment of forward-turning-forward locomotion is realized and evaluated, as shown in Fig. 17. Experimental states of the microrobot which is turning left are shown in Fig. 17a. The microrobot moves forward along X axis toward the center by rotating motion or fin motion, as shown in Fig. 17b. Secondly, the plane of rotational magnetic field is rotated by

Fig. 14 Whole control system
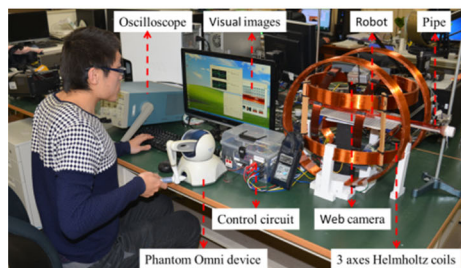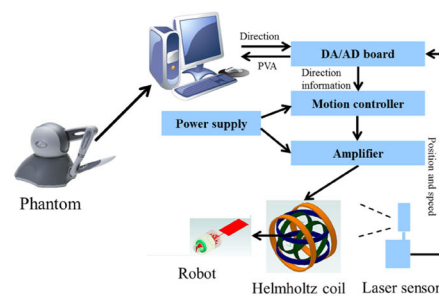
(a) Experimental setup   (b) Schematic diagram of the control system

counter-clockwise (CCW), the microrobot turns left at branch point, as shown in Fig. 17c. Finally, the microrobot moves forward along Y axis as shown in Fig. 17d. In the same way, the plane of rotational magnetic field is rotated by clockwise (CW), the microrobot turns right at branch point. Experiment of backward-turning-forward locomotion is also conducted and evaluated.

5.2 Experimental results and discussions

The relationships between the propulsive force, moving speed and frequency are indicated in Fig. 18. The experimental results implied that when the hybrid microrobot with spiral jet motion move from 10 to 40Hz, the moving speed is increasing with the propulsive force increasing. The maximum propulsive force is 5.4mN. The performance of hybrid motion microrobot in water is evaluated in water. The experimental results show the fin motion and the spiral jet motion work in different frequency, as shown in Fig. 19. The hybrid microrobot can move using the fin motion below 10Hz. The maximum moving speed is 4.74 mm/s. And it can move using the fin motion or spiral jet motion from 10 to 25 Hz by controlling the rotational magnetic field. The maximum speed of the fin motion is 7 mm/s at 14 Hz. While the frequency is above 25Hz, the hybrid microrobot moves using the spiral jet motion. Additionally, the performance is evaluated in oil to prove the microrobot is able to move in a high viscosity liquid, and the result is shown in Fig. 20. The maximum moving speed is 0.22 mm/s in oil. According to these results, we did an experiment of hybrid motion by adjusting the rotational magnetic field. The experimental results of forward with fin motion (FF), stop motion (S), forward with spiral jet motion (FS) and backward with spiral jet motion (BS) are shown in Fig. 21.

In this experimental result of spiral jet motion, there are two phenomena of interest. One is the initial

Fig. 15 Moving state in horizontal direction. (**a**) and (**b**) are forward motion with fin motion. (**c**) and (**f**) are stop motion. (**d**) and (**e**) are forward motion with spiral jet motion. (**g**) and (**h**) are backward motion with spiral jet motion
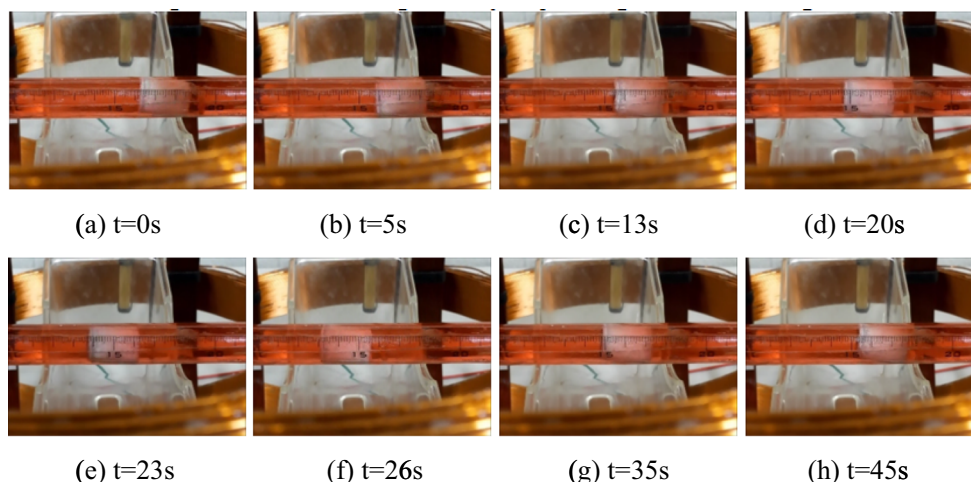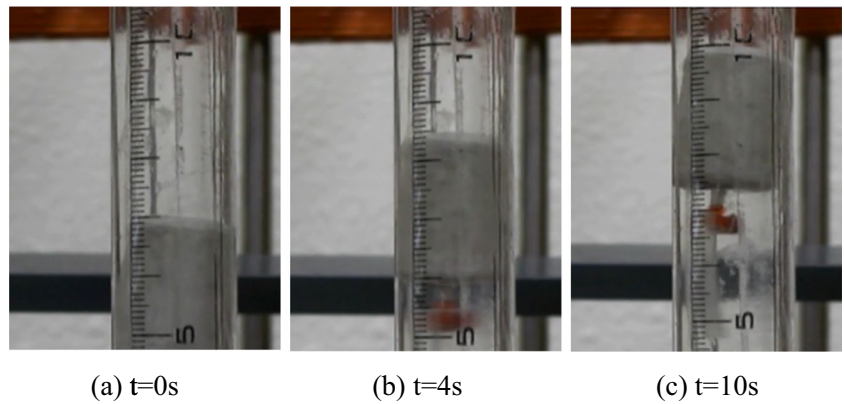

(a) t=0s   (b) t=5s   (c) t=13s   (d) t=20s

(e) t=23s   (f) t=26s   (g) t=35s   (h) t=45s

Fig. 16 Moving state in vertical direction

(a) t=0s   (b) t=4s   (c) t=10s

frequency (10Hz). It means that the hybrid microrobot generates enough propulsion to overcome resistance of fluid at this frequency. The other one is step out frequency (40Hz) that means the frequency above which the microrobot can no longer rotate continuously in synchronous with the rotational magnetic fields. Step-out frequency is well understood for magnetic helical microrobots in uniform fields, it is discussed in our previous researches. The experimental results of the spiral jet motion indicated the linearity between magnetic field changing frequency and the moving speed from 10 to 40Hz. The approximate numerical formula of spiral jet motion is shown in Eq. (18). Because the correlation coefficient is 0.9693, it has a high correlation. The

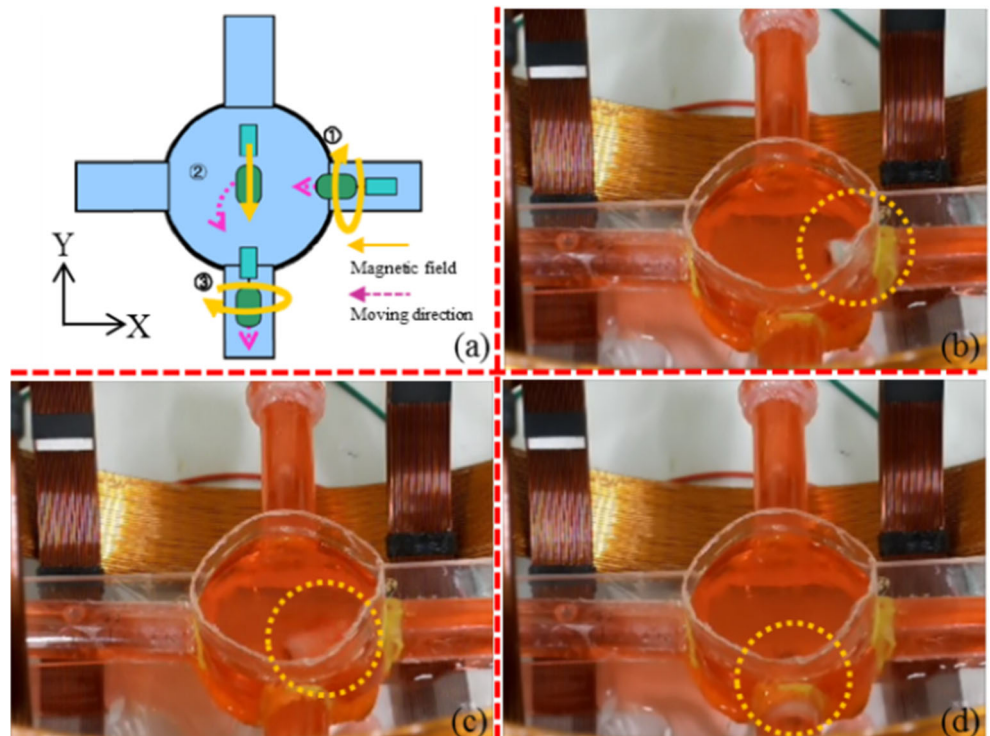approximate numerical formula of fin motion is shown in Eq. (19).

$$v_{spiral}(f) = 0.08921f - 0.4737 \tag{18}$$

$$v_{fin}(f) = -0.03279f^2 + 0.8229f \tag{19}$$

6 Conclusions

In this paper, to increase the dynamic efficiency and adapt this EMA system to use in various working environments, a novel magnetically actuated hybrid

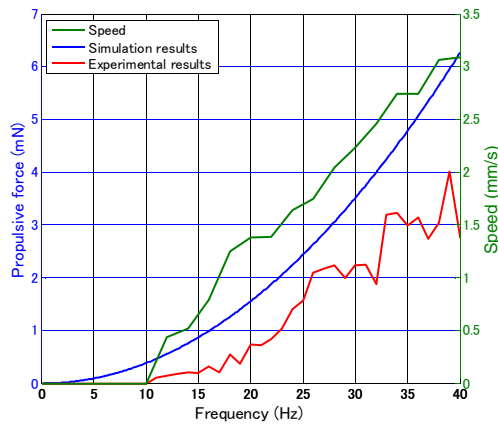Fig. 17 Forward-turning-forward locomotion

Fig. 18 Relationships between propulsive force, moving speed and frequency

microrobot with spiral jet motion and fin motion is proposed. The structure and mechanisms of hybrid motion (spiral jet motion and fin motion) are analyzed. And then major part of EMA system which is 3 axes Helmholtz coils is analyzed, designed and evaluated performance, in order to realize flexible control the hybrid microrobot. Finally, the motion characteristics of hybrid microrobot are evaluated and the hybrid realized the multi-DOFs locomotion in pipe. The experimental results indicated a number of advantages of the hybrid microrobot as follows:

1. The hybrid microrobot has a compact structure and wireless power supply and a small size.
2. The hybrid microrobot with one actuator can be driven to realize hybrid motion by a rotational magnetic field.
3. The hybrid motion can be controlled separated without any interference. In addition, the fin can improve the dynamic characteristic and reduce the shake which caused by the axial propulsive force for at the spiral jet motion.
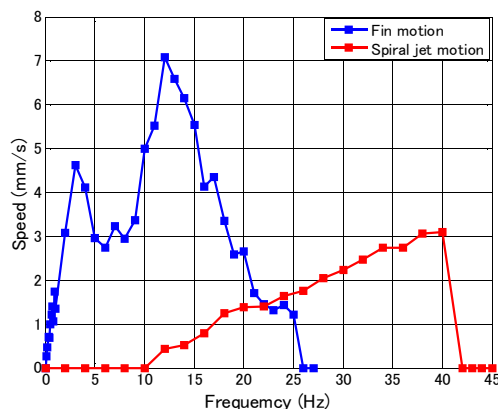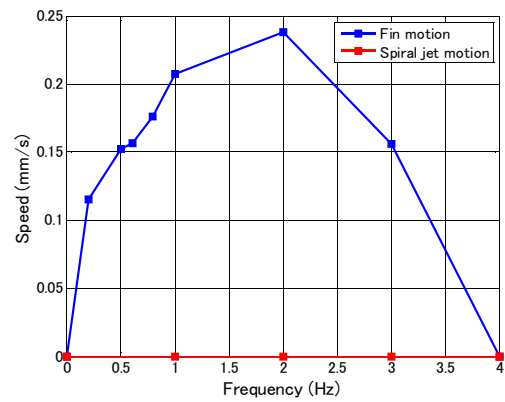

Fig. 20 Hybrid motion in oil

4. The hybrid microrobot can move in different environment by adjusting the hybrid motion or fin motion at different frequency. By adjusting the magnetic field changing frequency, the moving speed is controlled. The maximum speed of spiral jet motion is 4.74 mm/s and the maximum speed of fin motion is 7 mm/s.
5. Experimental results indicated the hybrid microrobot realize flexible motion in pipe by adjusting the magnetic field changing direction. Such as, horizontal motion, vertical motion, turning motion and so on.

Future work of this research will focus on optimizing the structure to increase propulsive force. In addition, the propulsive force can be limited at high frequency due to the dynamics of the 3 axes Helmholtz coils system and natural frequency, the actuation frequency also should be improved. And also, the real time image should be feedback to operators for an accurate control about moving speed and direction of hybrid microrobot. It has a potential capability to satisfy the requirements for medical applications.
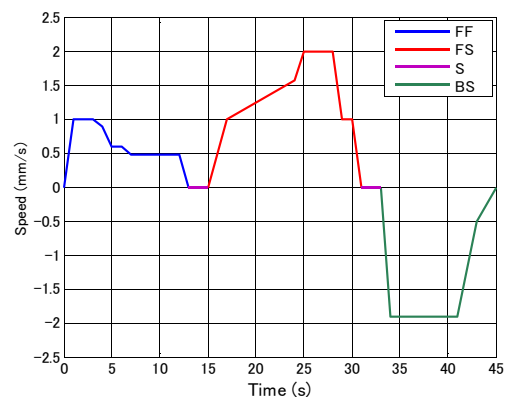

Fig. 19 Hybrid motion in water

Fig. 21 Forward-stop-backward motion

References

M.R. Basar, F. Malek, M.J. Khairudi, M. Shaharom Idris, I.M. Saleh, Int. J. Antennas Propag. **2012**, 1–14 (2012)

B. Behkam and M. Sitti, 2005 IEEE/ASME International Conference on Advanced Intelligent Mechatronics, 37–42, (2005)

H. Choi, J. Choi, S. Jeong, C. Yu, J. Park, S. Park, Smart Mater. Struct. **18**(11), 1–6 (2009)

Q. Fu, S. Guo, Y. Yamauchi, 2014 I.E. International Conference on Mechatronics and Automation, pp. 1995–2000, (2014).

B. Gao, S. Guo, X. Ye, Int. J. Mechatron. Autom. **1**(2), 79–89 (2011)

S. Guo, T. Fukuda and K. Asaka, IEEE International Conference on Robotics and Automation, 738–743, (2002)

S. Guo, T. Fukuda, K. Asaka, IEEE/ASME Trans. Mechatronics **8**(1), 136–141 (2003)

S. Guo, Q. Pan, M.B. Khamesee, J. Microsyst. Technol. **14**(3), 307–314 (2008)

S. Guo, Q. Fu, Y. Yamauchi, C. Yue, 2013 I.E. International Conference on Mechatronics and Automation, 831–836, (2013)

J. Guo, S. Guo, X. Wei, Y. Wang, Int. J. Adv. Robot. Syst. **11**, 1–13 (2014)

T. Honda, T. Sakashita, K. Narahashi, J. Yamasaki, J. Magn. Society of Japan **4**(4–2), 1175–1178 (2001)

S. M. Jeong, H. C. Choi, S. Y. Ko, J. O. Park, and S. H. Park. IEEE International Conference on Biomedical Robotics and Biomechatronics, 482–487, (2012)

H. Keller, A. Juloski, H. Kawano, M. Bechtold, A. Kimura, H. Takizawa, R. Kuth, 2012 4th IEEE RAS & EMBS International Conference on Biomedical Robotics and Biomechatronics (BioRob), 859 – 865, (2012)

B. Kim, S. Lee, J.H. Park, J.O. Park, IEEE/ASME Trans. Mechatronics **10**(1), 77–86 (2005)

N. Mir-Nasiri, H. Siswoyo Jo, Int. J. Mechatronics Automation **1**(2), 132–142 (2011)

A. Moglia, A. Menciassi, M.O. Schurr, P. Dario, Biomed. Microdevices **9**(2), 235–243 (2007)

A. Nacci, F. Ursino, R. La Vela, F. Matteucci, V. Mallardi, B. Fattori, Acta Otorhinolaryngol. Ital. **28**(4), 206–211 (2008)

T. Okada, S. Guo, Q. Fu and Y. Yamauchi, 2012 ICME International Conference on Complex Medical Engineering, 306–311, (2012)

T. Okada, S. Guo, X. Nan, Q. Fu and Y. Yamauchi, 2012 I.E. International Conference on Mechatronics and Automation, 2405–2410, (2012)

Q. Pan and S. Guo, 2007 I.E. International Conference on Robotics and Automation, 187–192, (2007)

Q. Pan and S. Guo, 2009 I.E. International Conference on Robotics and Automation, 2995–3000, (2009)

Q. Pan, S. Guo, T. Okada, Int. J. Mechatronics and Automation **1**(1), 60–69 (2011)

X. Wang, M.Q.-H. Meng, Int. J. Mechatronic Autom **1**(1), 38–45 (2011)

L. Wang, G. Zhang, J.C. Luo, F. Zeng, Q.Z. Wang, S.A. Alfano, A. Katz, M. Zevallos, R.R. Alfano, Biomed. Microdevices **7**(2), 111–115 (2005)

K.B. Yesin, K. Vollmers, B.J. Nelson, Int. J. Robot. Res. **25**(5–6), 527–536 (2006a)

K.B. Yesin, K. Vollmers, B.J. Nelson, Springer Tracts in Advanced Robotics **21**, 321–330 (2006b)

S. Yim, M. Sitti, Trans. Robot. **28**(1), 183–193 (2012)

C. Yu, J. Kim, H. Choi, J. Choi, S. Jeong, K. Cha, J. Park, S. Park, Sensors Actuators A Phys. **161**, 297–304 (2010)

L. Zhang, J.J. Abbott, L.X. Dong, K.E. Peyer, B.E. Kratochvil, H.X. Zhang, C. Bergeles, B.J. Nelson, Nano Lett. **9**(10), 3663–3667 (2009)